Journal of the Electrochemical Society

Calendar Aging of Lithium-Ion Batteries

Calendar Aging of Lithium-Ion Batteries

I. Impact of the Graphite Anode on Capacity Fade

Peter Keil,[a,*,z] Simon F. Schuster,[a] Jörn Wilhelm,[a,*] Julian Travi,[a] Andreas Hauser,[b] Ralph C. Karl,[a] and Andreas Jossen[a,b]

[a]*Institute for Electrical Energy Storage Technology, Technical University of Munich (TUM), Munich, Germany*
[b]*TUM CREATE Ltd., Singapore*

In this study, the calendar aging of lithium-ion batteries is investigated at different temperatures for 16 states of charge (SoCs) from 0 to 100%. Three types of 18650 lithium-ion cells, containing different cathode materials, have been examined. Our study demonstrates that calendar aging does not increase steadily with the SoC. Instead, plateau regions, covering SoC intervals of more than 20%–30% of the cell capacity, are observed wherein the capacity fade is similar. Differential voltage analyses confirm that the capacity fade is mainly caused by a shift in the electrode balancing. Furthermore, our study reveals the high impact of the graphite electrode on calendar aging. Lower anode potentials, which aggravate electrolyte reduction and thus promote solid electrolyte interphase growth, have been identified as the main driver of capacity fade during storage. In the high SoC regime where the graphite anode is lithiated more than 50%, the low anode potential accelerates the loss of cyclable lithium, which in turn distorts the electrode balancing. Aging mechanisms induced by high cell potential, such as electrolyte oxidation or transition-metal dissolution, seem to play only a minor role. To maximize battery life, high storage SoCs corresponding to low anode potential should be avoided.
 [DOI: 10.1149/2.0411609jes] All rights reserved.

Manuscript submitted March 15, 2016; revised manuscript received May 20, 2016. Published July 6, 2016.

Calendar aging comprises all aging processes that lead to a degradation of a battery cell independent of charge-discharge cycling. It is an important factor in many applications of lithium-ion batteries where the operation periods are substantially shorter than the idle intervals, such as in electric vehicles. Furthermore, the degradation owing to calendar aging can also be predominant in cycle aging studies, especially when cycle depths and current rates are low.[1]

In contrast to cycle aging, where mechanical strain in the electrode active materials[2–4] or lithium plating[5–9] can cause severe degradation, the predominant mechanism of calendar aging is the evolution of passivation layers at the electrode–electrolyte interfaces.[10–12] The formation, growth, or reconstruction of passivation layers consume cyclable lithium as a result of electrolyte decomposition, i.e., reduction at the anode and oxidation at the cathode interface.[13,14] Furthermore, the growth of the passivation layer at the anode, which is usually referred to as the solid electrolyte interphase (SEI), is said to be additionally catalyzed by dissolved transition-metal ions from the cathode, which are in turn reduced again to metals at the anode.[15,16] Basically, both the evolution of passivation layers and transition-metal dissolution are promoted by a high state of charge (SoC) and temperature.[13,14]

As these are the main drivers of calendar aging, continuously accelerated degradation with an increase of the storage SoC and temperature is commonly assumed for lithium-ion cells with graphite anodes and transition-metal-layered cathodes. Whereas lithium loss is generally ascribed to the evolution of the SEI, the passivation layer at the cathode is associated with rising impedance.[15] As the evolution of the SEI is driven by the respective potential of the anode with regard to the electrochemical stability of the electrolyte solvent and conducting salt(s), a continuously accelerated capacity fade with an increase of the storage SoC is disputable in the case of the staging phenomenon in graphite.[2,17] Thus, even if the effect of transition-metal dissolution continuously increases with higher storage SoC, the cell capacity fade due to calendar aging should exhibit plateaus corresponding to the respective stages of the graphite potential when SEI evolution is the predominant aging mechanism.

There are many studies on calendar aging of lithium-ion batteries and they all reported accelerated aging at higher SoCs. However, these studies usually considered only a few storage SoCs or storage voltages. Most of the studies examined only three different values or fewer,[18–28] and there is one study that investigated five SoCs from 20% to 100%.[29] Hence, none of these studies covered the entire SoC range from 0 to 100% and none are able to thoroughly report the relationship between SoC and capacity fade.

Only Ecker et al.[30] investigated calendar aging with a finer SoC resolution; they examined the aging of NMC lithium-ion cells at 12 storage voltages. A correlation between the capacity fade and the graphite stages was identified. Since the correlation between open circuit voltage and SoC changes with aging, the SoCs of cells examined with a predefined voltage level tend to drift with increasing capacity fade.[31] This impedes the assignment of the aging results to explicit SoC values which represent a certain ratio of stored ampere-hours to cell capacity. Moreover, it prevents a robust analysis of storage SoCs close to the potential steps of the graphite anode when the balancing of the electrodes shifts due to a loss of cyclable lithium.

Consequently, to further examine and verify the impact of the graphite electrode on the calendar aging of lithium-ion batteries, we conducted an experimental aging study with different lithium-ion chemistries and with a fine SoC resolution in which the storage SoCs were always related to the actual cell capacity instead of being defined as voltage levels.

Experimental

For this paper, we performed an extensive calendar aging study with special focus on the dependency of the storage SoC on capacity degradation. We used differential voltage analysis (DVA) to identify interdependencies between the electrode balancing and calendar aging. This section presents the different lithium-ion cells and storage conditions examined in our aging study. Furthermore, the test procedure and the fabrication of coin cells for supporting half-cell measurements are described.

Lithium-ion cells.—For our experimental investigations on calendar aging, three types of commercial 18650 cells with different cathode materials were selected. To minimize the impact of stochastic variations, cells from identical production lots were examined. As shown in Table I, the cells all contain graphite anodes and have NCA, NMC, and LFP cathodes. Their capacities range between 1.1 and 2.8 Ah. In addition to the minimum and maximum operating voltages (V_{min} and V_{max}), Table I also compares the coated electrode areas of the three cell types. Cathode areas are presented, as they are generally somewhat smaller than anode areas. Although the capacities differ by a factor of up to 2.5, the electrode areas are rather similar. This leads to

*Electrochemical Society Member.
[z]E-mail: peter.keil@tum.de

Table I. Properties of the investigated types of lithium-ion cells.

	NCA cells	NMC cells	LFP cells
Manufacturer	Panasonic	Sanyo	A123
Model	NCR18650PD	UR18650E	APR18650M1A
Nominal Capacity (C_N)	2.8 Ah	2.05 Ah	1.1 Ah
Maximum Voltage (V_{max})	4.2 V	4.2 V	3.6 V
Minimum Voltage (V_{min})	2.5 V	2.75 V	2.0 V
Anode Material	Graphite	Graphite	Graphite
Cathode Material	$LiNiCoAlO_2$	$LiNiCoMnO_2$	$LiFePO_4$
Coated Area* (A_c) (double-sided coating)	2 × 667 mm × 57.5 mm = 767 cm^2	2 × 690 mm × 57.0 mm = 787 cm^2	2 × 710 mm × 55.5 mm = 788 cm^2
Areal Capacity (C_N/A_c)	3.65 mAh cm^{-2}	2.6 mAh cm^{-2}	1.4 mAh cm^{-2}

*Cathode areas, as they are slightly smaller than the anode areas.

differences in areal capacities, which are also listed in Table I. Since the cells all have a similar volume due to the 18650 form factor and since the capacity variations are substantially larger than the differences in the specific capacities of the three cathode materials,[32] the differences in capacity must origin mainly from different electrode porosities and thicknesses.

To obtain comparable results for the three cell types, identical absolute current values instead of identical C-rates were used in our measurement procedures. Due to the similar electrode areas, the identical absolute current values provided similar current densities (A cm^{-2}) for all cells. As demonstrated by the areal capacity values in Table I, using identical C-rates would have caused higher current densities for the cells with higher capacity. Thus, the high-energy NCA cells would have been exposed to a current density 2.6 times as high as for the high-power LFP cells. Hence, they would have been disproportionately stressed by the higher current density. This confirms that when using identical C-rates for cells of the same size, cells with a higher energy content may be penalized for their higher capacity.[33] Consequently, identical absolute current values were preferred in this aging study.

Storage conditions.—To investigate calendar aging, cells were stored at different SoCs and at different temperatures. In this paper, the SoC is always regarded as the stored amount of charge Q_{stored} with respect to the actual cell capacity C_{actual}:

$$SoC = Q_{stored}/C_{actual} \quad [1]$$

In total, 16 storage SoCs from 0 to 100% were examined. The investigated storage SoCs comprised all multiples of 10% and additionally 5%, 45%, 55%, 65%, and 95% to obtain a finer resolution at very low SoC, at very high SoC, and in the medium SoC range, for which substantial changes in calendar aging were reported in previous aging studies.[30,34] These 16 SoCs were examined at storage temperatures of 25°C, 40°C, and 50°C.

Test procedure.—To monitor the degradation of the cells, a uniform checkup procedure was performed periodically at 25°C for all cells. As listed in Table II, this checkup comprised a constant current (CC) charging step with a low charging current of 100 mA for DVA and a constant current constant voltage (CCCV) discharging step to measure C_{actual}. In this paper, charging currents have positive values whereas discharging currents are represented by negative values.

Table II. Checkup sequence at 25°C, containing steps for differential voltage analysis (3) and capacity measurement (5).

Step	Parameters	Termination
1 Discharge CCCV	I = –1 A, V = V_{min}	I > –0.1 A
2 Pause		t > 15 min
3 Charge CC	I = 100 mA	V > V_{max}
4 Pause		t > 15 min
5 Discharge CCCV	I = –2 A, V = V_{min}	I > –0.1 A
6 Pause		t > 15 min
7 Charge CC	I = 700 mA	SoC > 50%

DVA is an advanced technique for electrical characterization of battery cells. From a constant current charging or discharging sequence, the derivative dV/dQ is computed, which represents a linear superposition of the anode and cathode derivative.[35] Hence, a differential voltage spectrum can be used to identify the balancing and the utilization of the two electrodes without inserting a reference electrode.[36] In aging studies, DVA allows the separation of anode degradation, cathode degradation, and shifts in the electrode balancing due to a loss of cyclable lithium.[37,38] Figure 1 shows the low-current charging curves and the resulting differential voltage spectra for the three cell types in the new state. For all three cell types, the charging current of 100 mA corresponds to a current density of approximately 0.13 mA cm^{-2} for each side of the double-sided electrodes.

Furthermore, discharge pulses from 0 A to –3 A with a duration of 10 s were evaluated at 50% SoC to identify changes in the cell resistance. $R_{dc,10s}$ was obtained from the cell voltage immediately

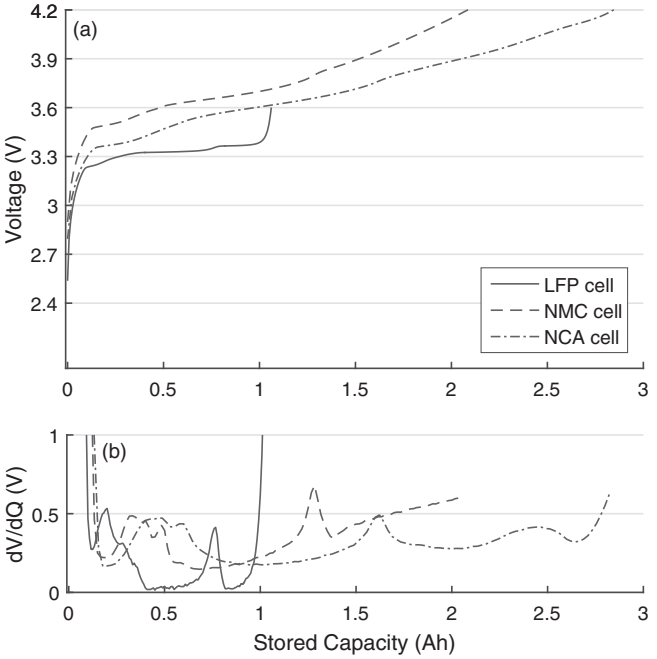

Figure 1. (a) Voltage curves over stored capacity for low-current charging with 100 mA; (b) the resulting differential voltage spectra.

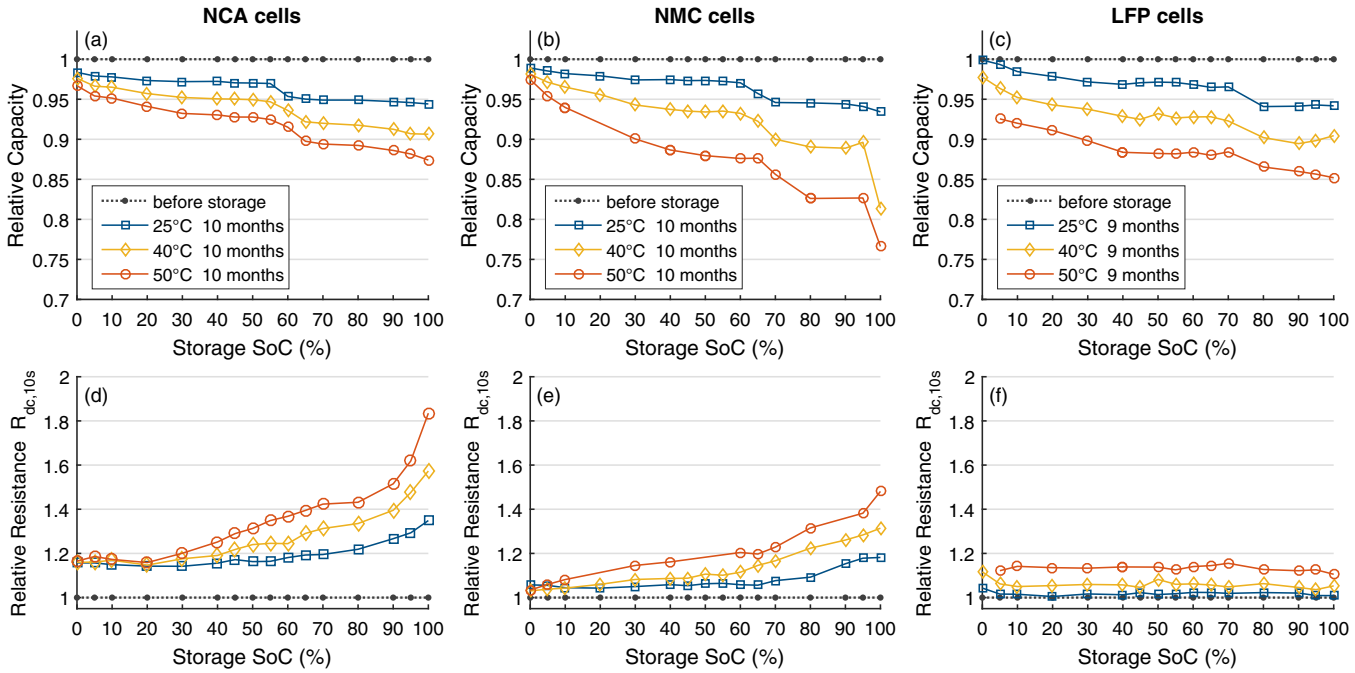

Figure 2. Battery degradation after ca. 9–10 months of storage at various SoCs and different temperatures: (a-c) capacity fade; (d-f) rise of internal resistances.

before the pulse (V_{0s}) and at the end of the pulse (V_{10s}).

$$R_{dc,10s} = (V_{10s} - V_{0s}) / -3A \quad [2]$$

After the checkup procedure, the cells were brought to storage SoC. The standard procedure for this was charging the cells with Q_{charge} from the completely discharged state to the storage SoC:

$$Q_{charge} = SoC \cdot C_{actual} \quad [3]$$

The distribution of the lithium atoms in the electrodes is supposed to vary for different charge-discharge histories. Regarding the cell potential, this becomes apparent by a hysteresis in the open circuit voltage between charging and discharging to the same SoC, which amounts to 10–20 mV.[39–42] For graphite electrodes, different lithium distributions for the same SoC have also been confirmed by electro-optical measurements.[43] To study the dependence of calendar aging on the charge-discharge history, an alternative procedure for reaching the storage SoC was examined, i.e., discharging $Q_{discharge}$ from the fully charged cells to reach the storage SoC.

$$Q_{discharge} = -(1 - SoC) \cdot C_{actual} \quad [4]$$

The checkup procedure was performed with a BaSyTec CTS battery test system containing 32 individual 5 V/±5 A test channels and the cells were tested inside a 25°C thermal chamber. After the checkup, all cells were brought to the respective storage SoC at 25°C before they were stored in thermal chambers with constant temperatures of 25, 40, and 50°C.

Coin cells.—To study the behavior of the individual electrodes and to verify the balancing of the electrodes in the commercial full-cells obtained by DVA, coin cells were built from the respective active materials. For each cell type, one cell at 0% SoC and one cell at 100% SoC was opened. The jelly roll was extracted and electrode samples with a diameter of 14 mm were punched out for 2032-sized coin cells. The samples were used to build half-cells together with metal lithium electrodes with a diameter of 15 mm. For the fabrication of the coin cells, fiberglass separators with a diameter of 16 mm and ca. 160 µl of fresh electrolyte (1 M $LiPF_6$ in EC:EMC (3:7) + 2% VC) were used.

Single-sided anode samples could be extracted from the NMC and NCA cells, since the outermost anode winding was coated only on the inner side. Hence, no side effects from the back side of the electrode sample occurred during the measurements. All other electrode samples had double-sided coatings, for which capacity drifts due to an interfering back side coating had to be expected during cycling.[44]

For the coin cells, similar current densities as for the DVA measurement of the commercial cells were applied. Thus, the charging and discharging currents were defined as follows:

$$I_{coin} = \pm(1.4\ \text{cm}/2)^2 \cdot \pi \cdot 0.13\,\text{mAcm}^{-2} = \pm 0.2\,\text{mA} \quad [5]$$

All coin cell measurements were performed at 25°C. The graphite half-cells were cycled between 0.1 and 1.5 V, the NCA and NMC half-cells between 2.5 and 4.3 V, and the LFP half-cells between 2.0 and 3.7 V. Before the charge-discharge cycling, the coin cells were stored for at least 12 h to provide sufficient time for the electrolyte to soak into the pores of the active material and the separator.

The half-cell profiles were used to reconstruct the full-cell voltage characteristics and enable correlation between the plateaus in the anode potential and the capacity fade of the commercial lithium-ion cells.

Results and Discussion

The focus of this paper is the dependency of the capacity fade on storage SoCs. Changes of the internal resistances are only presented briefly, as they will be examined thoroughly in a separate article. The following sections present and discuss the impact of the anode potential on calendar aging.

General aging behavior.—For the three types of lithium-ion cells examined, Figures 2a–2c show the capacity fade after a storage period of 9–10 months. As expected, they all exhibit an increased calendar aging with higher storage temperature. However, no steadily increasing degradation with SoC is observed. Instead, there are plateau regions, covering SoC intervals of more than 20%–30% of the cell capacity, in which the capacity fade is similar. A marked step in the capacity curves is observed at about 60% SoC for the NCA and NMC cells and above 70% SoC for the LFP cells. For the observed relationships between storage SoC and capacity fade, no simple linear, polynomial, or exponential approximations are possible without considerable deviation in certain SoC regions. Hence, the measurement of calendar

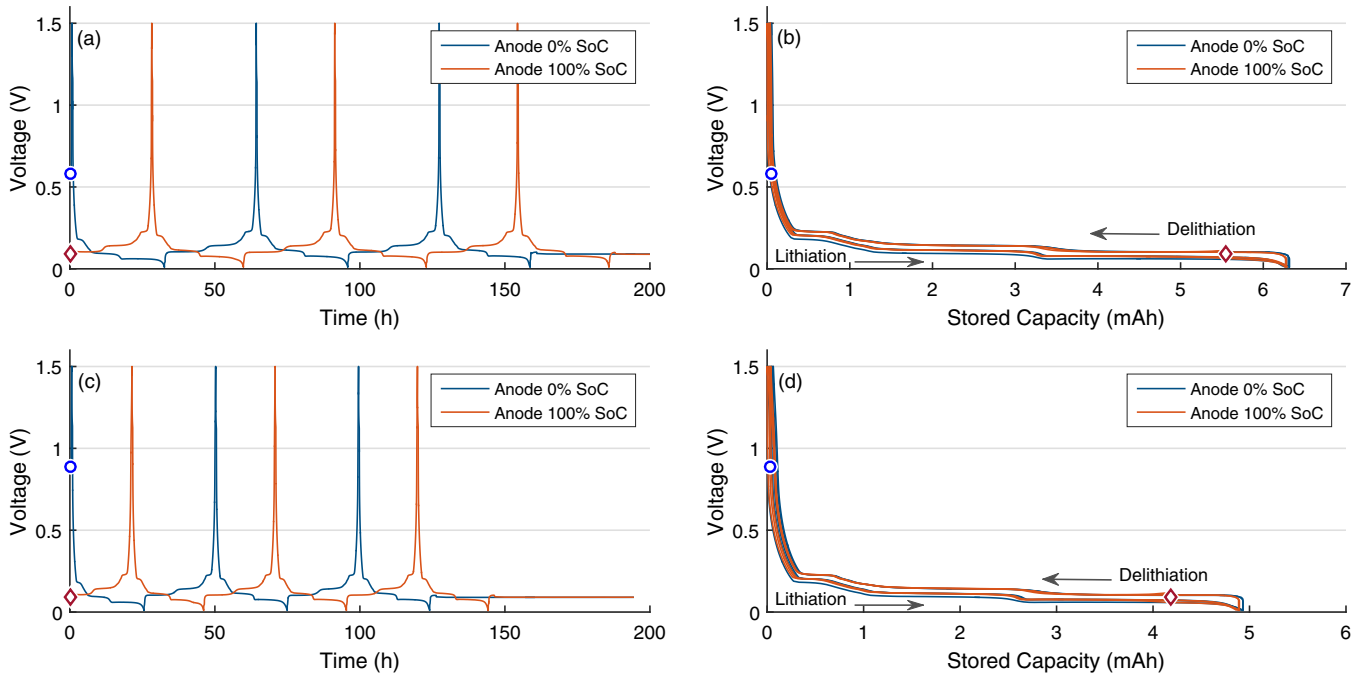

Figure 3. Three charge-discharge cycles of the graphite half-cells from an empty (0% SoC) and a full (100% SoC) NCA and NMC cell in new condition. (a, c) Voltage over time; (b, d) voltage over stored capacity. Markers indicate the potential and the stored capacity of the graphite anodes for the full-cells at 0% (blue circles) and 100% SoC (red diamonds).

aging for only three SoCs, as is the case in most publications, is not sufficient to precisely describe calendar aging with respect to the SoC when the qualitative characteristics over the entire SoC range are not known.

Figure 2 also reveals different storage durations for the three cell types owing to variations in the checkup schedules of the different cell types. The 9 months of storage of the LFP cells are shorter than the storage periods of the NCA and NMC cells. To estimate the capacity fade of the LFP cells for 10 months of storage, the derivative of the capacity fade with respect to time has been evaluated after 9 month of storage. It amounts to ca. 0.2 percentage points of capacity fade per month at 25°C and to ca. 0.5 percentage points per month at 50°C. Adding this additional capacity fade to the capacity curves depicted in Figure 2c enables a better comparability of the three cell types. The capacity curves of the different cell types then show that in the medium SoC region (around 50% SoC), the capacity fade is largest for the LFP and NMC cells, especially at higher storage temperatures of 40°C and 50°C.

For storage at 50°C and SoCs above 70%, the NMC cells exhibit a higher capacity fade than the NCA and LFP cells. A similar aging behavior for the NMC cells has already been reported by Ref. 30, in which calendar aging at 50°C revealed a substantially increasing capacity fade at 100% SoC and a somewhat lower capacity fade at 95% SoC compared with that at 80%–90% SoC.

The changes in cell resistance after 9–10 months of storage are shown in Figures 2d–2f. The resistance increase for the LFP cells is lowest and also largely independent of the storage SoC. For the NCA and NMC cells, resistances increase with higher storage SoC and no plateaus similar to the capacity fade are observed. For the NCA cells, the resistance increase is constant between 0 and 30% SoC, where the capacity fade increases notably, and the resistance increase accelerates substantially above 90% SoC, where the capacity fade only slightly increases.

For all three types of lithium-ion cells examined, there is no direct correlation between capacity fade and resistance increase. Particularly, the step in capacity fade observed at ca. 60%–70% SoC is not reflected in the resistance change. Half-cell investigations with coin cells and DVA are performed in the subsequent sections to demonstrate that this step in capacity fade is attributable to the potential of the graphite anode.

Potential and utilization of the graphite anode.—To describe possible interdependencies between calendar aging and the graphite potential, the balancing of the cells has been examined with coin cells fabricated from the electrode material of the commercial full-cells in the new condition. At least three half-cells were fabricated from each electrode material. Since the cycling behavior was highly reproducible, the results of only one half-cell sample are presented.

For the NCA and NMC cells, Figures 3a, 3c show three charge-discharge cycles of the graphite anode half-cells, which were performed with low currents of 0.2 mA to clearly obtain the different voltage plateaus. Each charge or discharge step has a duration of up to 32 h for the anode coin cells from the NCA cells and up to 25 h for the coin cells from the NMC cells. In Figures 3b, 3d, the same half-cell voltage data is plotted versus stored capacity. Since these coin cells contain electrode samples with only single-sided coatings, the three cycles are rather similar and no capacity drifts occur. For the anode coin cells of the LFP cells and all cathode coin cells, a capacity drift was observed, especially for the first charge-discharge cycle due to an interfering back side coating. From these coin cells, only the last charging or discharging sequence has been used for the reconstruction of the full-cell spectra. In Figures 3b and 3d, the circle and diamond markers indicate the initial potential and stored capacity of the half-cells after the fabrication process. The blue circles show that a 0% SoC of the full-cell correlates with a completely delithiated anode. For the full-cells at 100% SoC, the anode is not completely lithiated. The red diamonds in Figures 3b and 3d illustrate the utilization of the oversized graphite anodes. At ca. 50% of the maximum storage capacity, a potential step can be observed, which indicates a different staging configuration of the intercalated lithium. Above 50% lithiation, the two-phase regime of LiC_{12} and LiC_6 can be observed.[2,45]

Reconstruction of full-cell behavior from half-cell spectra.—To investigate the transitions between different phase equilibria, DVA has been used. It also allows to reconstruct the full-cell behavior from

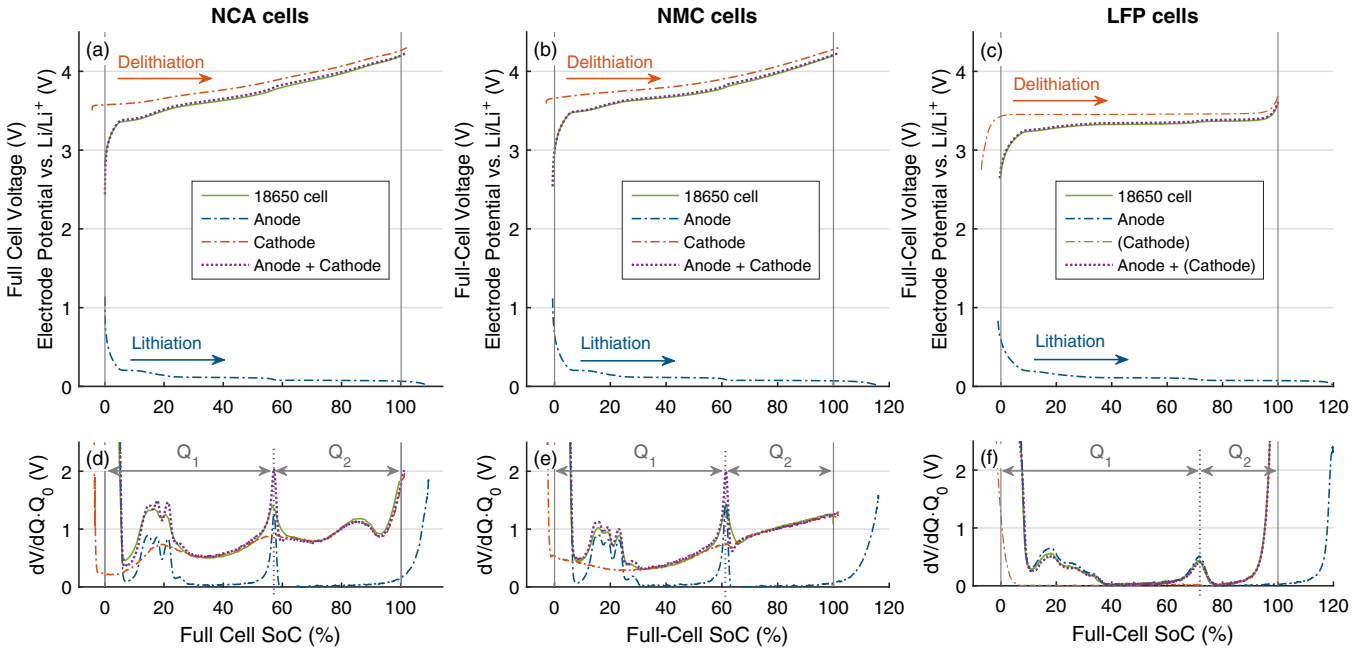

Figure 4. Reconstruction of the full-cell voltage of a new cell and the differential voltage spectrum from half-cell data. (a-c) Voltage behavior for low-current charging; (d-f) differential voltage spectra with the central graphite peak highlighted by the dotted vertical line, which separates the actual capacity into two characteristic capacity values Q_1 and Q_2. Q_1 is an indicator for graphite degradation and Q_2 is an indicator for shifts in the electrode balancing.

half-cell data, which helps to identify the different staging regimes for the full-cells without opening the cells.

For all three cell types, Figure 4 illustrates the reconstruction of the full-cell voltage and the differential voltage spectrum by linear superposition from half-cell data of the anode and the cathode. Figures 4d–4f show that slopes and peaks of the individual electrodes can be clearly recognized in the full-cell spectrum. Hence, the differential voltage spectra contain valuable information on the scaling and balancing of the two electrodes. An excellent agreement between half-cell data and full-cell behavior can be achieved in the reconstruction process, especially when using the differential voltage spectra for scaling and shifting the individual contributions of the anode and cathode half-cell.

As already described in the previous section, Figures 4a–4c also show that the decreasing cell voltage indicating 0% SoC is generally caused by the rising potential of the delithiated graphite anode. Hence, an empty anode determines the lower end of the capacity window usable for charge-discharge cycling. The upper end of the usable capacity window is not determined by the graphite anode, since it is oversized. Thus, the upper end is determined by the increasing potential of the delithiated cathode.

The slopes and peaks in the differential voltage spectra help to correctly scale the capacities of the graphite anodes and the NCA and NMC cathodes in the reconstruction process. For the LFP cathode, however, no precise capacity scaling is possible due to the characteristic half-cell voltage of the LFP cathode, which is constant over a wide SoC range and exhibits notable changes only at very low and very high degrees of lithiation. Thus LFP only exhibits two slopes in the differential voltage spectrum and no further characteristic peaks. In the differential voltage spectrum of the full-cell, only the slope due to the rising potential of the LFP cathode toward 100% SoC can be identified. As the decreasing potential of the LFP toward the fully lithiated state is not reached in the full-cell, the second LFP slope does not become visible in the full-cell spectrum. Since no second reference mark could be determined for the horizontal scaling of the LFP curves, the scaling of the cathode data in Figure 4f is only an estimate, which is indicated by the parenthesis. For the graphite anodes, a correct capacity scaling has been possible for all three types of cell due to the numerous characteristic peaks in the differential voltage spectra.

Since the peak distances are proportional to the storage capacity of an electrode and since the peaks and slopes can be clearly assigned to the anode or cathode, DVA enables us to track the degradation of the electrodes and the shifts in the electrode balancing without opening the cells to insert a reference electrode or the need to perform post-mortem analyses. In Figures 4d–4f, the central graphite peak, which indicates a degree of lithiation of the graphite anode of about 50%, is highlighted. This peak divides the cell capacity C_{actual} into two characteristic capacities Q_1 and Q_2. Q_1, which represents the distance between 0% SoC and the central graphite peak, provides information about the storage capacity of the graphite anode. Q_2, which represents the distance between the central graphite peak and 100% SoC, provides information about the balancing of both electrodes. A change in Q_2 without a change of the anode and cathode capacity indicates a loss of cyclable lithium, also termed loss of lithium inventory, due to lithium-consuming side reactions. Since the differential voltage spectra of NMC and LFP do not contain characteristic peaks that can be easily evaluated, no third capacity value could be defined for monitoring changes in the cathode capacity. Hence, changes in cathode capacity have been evaluated by fitting the entire spectrum and analyzing the resulting capacity scaling factor of the cathode.

For all three cell types examined, the reconstruction of full-cell behavior from half-cell data has demonstrated how the effects of both electrodes add linearly and that changes in anode capacity and electrode balancing can be identified easily from changes in the differential voltage spectrum of the commercial full-cell.

Capacity fade versus anode potential.—The information on the balancing and utilization of the electrodes, which has been obtained by half-cell measurements and DVA, is now examined for correlations with calendar aging. Since we assume a considerable impact of the anode potential on capacity fade, both values are plotted versus SoC and opposed to each other in Figure 5.

It becomes obvious that in the plateaus of the highest capacity fade, the anode potential is lowest. For the NCA and NMC cells, the low anode potential starts at about 60% SoC and for the LFP cells, the low anode potential starts at about 70%. The medium anode potential between 30% and 60% SoC for the NCA and NMC cells and between 40% and 70% for the LFP cells correlates well with the

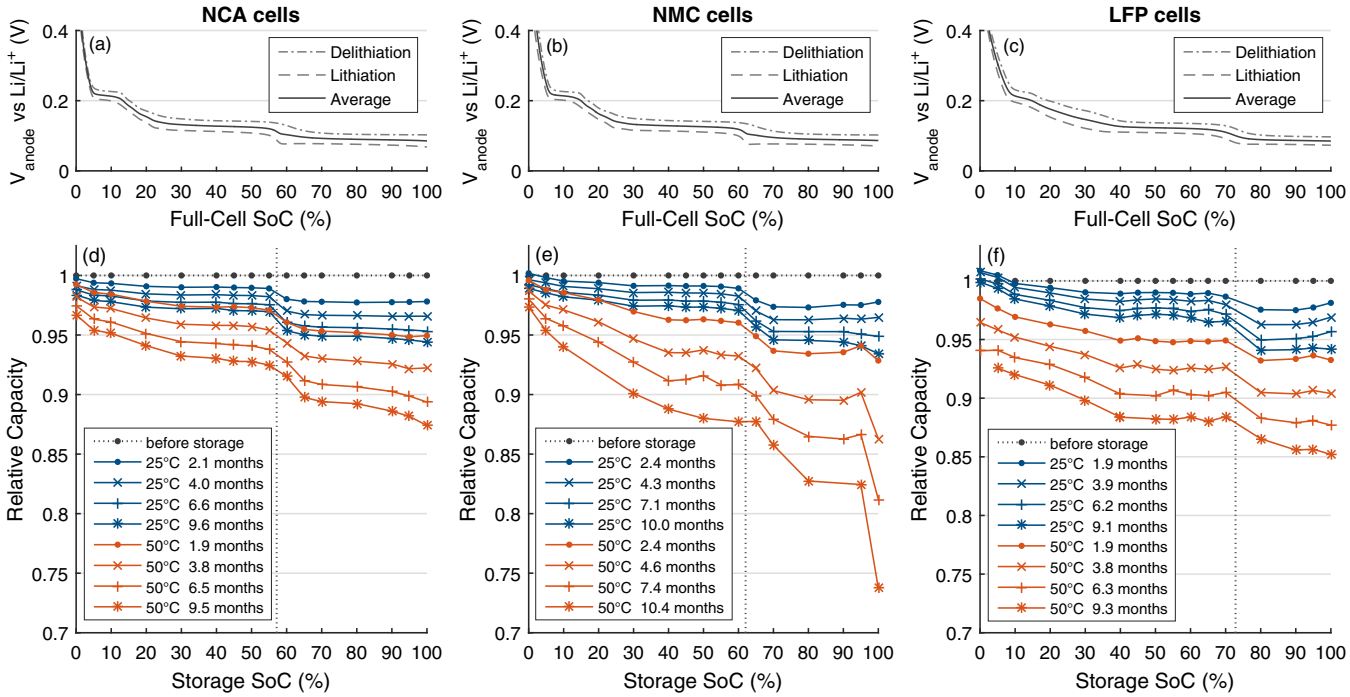

Figure 5. (a-c) Anode potential over SoC from half-cell measurements; (d-f) capacity fade over storage SoC for different storage periods. The location of the central graphite peak in the new condition is highlighted by a dotted vertical line.

medium capacity fade for these storage SoCs. In the low SoC regime below 30% or 40% SoC, the anode potential rises and the capacity fade diminishes.

These trends can be clearly observed in Figures 5d–5f for the cells stored at 25°C, where a sharp separation between the different aging regions can be observed. The transition from the plateau of medium capacity fade to the plateau of high capacity fade correlates particularly strongly with the position of the central graphite peak, indicating a degree of lithiation of ca. 50%. Hence, staying below this characteristic SoC can reduce calendar aging considerably.

For the cells stored at 50°C, the capacity fade is substantially higher. Moreover, the transition between the different aging plateaus is not as sharp as for the cells stored at 25°C. The reason for this will be discussed in the last result section, which focuses explicitly on this transition zone. Furthermore, some additional aging effects toward 100% SoC can be observed: The NCA cells exhibit a somewhat increasing capacity fade from 80% to 100% SoC; and the NMC cells reveal a steep increase in capacity fade for the 100% cell. As these effects do not correlate with the graphite potential, they are thought to be caused by side-reactions driven by high cell voltage, such as oxidation of the electrolyte and transition-metal dissolution, and higher degrees of delithiation of the cathode, which can deteriorate the lattice structure of the cobalt-oxide-based and nickel-oxide-based cathode materials.[3,46] This also explains why no additional capacity fade toward 100% SoC has been observed for the LFP cells, since their maximum voltage is considerably lower and the LFP lattice structure has a higher stability which allows complete delithiation.[47,48]

As illustrated in Figures 5d–5f, the location of the central graphite peak ranges between 57% SoC for the high-energy NCA cells and 73% SoC for the high-power LFP cells. The corresponding capacity fade curves demonstrate that the cell design of the high-power LFP cells, where the central graphite peak lies at a higher SoC, enables higher storage SoCs without reaching the region of fastest capacity fade.

For all three cell types, a continuously decreasing degradation over time is observed. The largest capacity fade occurs during the first weeks of storage and the overall trend exhibits a square-root-of-time behavior. This trend is in good correlation with SEI growth, for which a linear increase with the square root of time is generally assumed.[49,50] Overall, the results confirm a clear correlation between the anode potential and calendar aging of lithium-ion cells.

Electrode degradation and shift of electrode balancing.—In the previous section, an increasing capacity fade was reported for lower anode potentials. However, this information on capacity fade does not provide much information about the degradation mechanisms and origins of the capacity loss. Therefore, the DVA data are evaluated to separate between anode degradation, cathode degradation, and shifts in the electrode balancing caused by a loss of cyclable lithium.

The bars depicted in Figures 6a–6c show the capacity fade for six of the 16 storage SoCs and different temperatures. The entire bar length represents the remaining cell capacity C_{actual}, which is further separated into a dark-colored part, representing Q_1, and a light-colored part, representing Q_2.

Comparing the Q_1 values of aged cells with the reference value of new cells (dark gray bars) reveals zero (or very minor) degradation of the graphite anode, since the position of the graphite peak and, thus, the storage capability of the graphite anode has remained largely unchanged. Graphite degradation is only observed for the NMC cells stored at 100% SoC and at higher temperatures. Even for the cells exhibiting a certain loss of anode capacity, this loss is substantially smaller than the fade of the overall cell capacity. Furthermore, this capacity fade has not affected the cell capacity, since the anodes are generally oversized.

The reconstruction of the differential voltage spectra of aged cells with the half-cell profiles of anode and cathode has also indicated that there is zero (or very minor) cathode degradation. Thus, the loss of cyclable lithium can be confirmed as the major cause of capacity fade due to calendar aging. The resulting shift in the electrode balancing can be analyzed quantitatively from the decreasing Q_2 values.

Impact of charge-discharge history.—Figure 7 compares the capacity fades of two sets of NCA and NMC cells stored at 50°C with different charge-discharge histories. For both types of cell, the capacity curves exhibit a very good agreement between the two sets of cells. This confirms the low cell-to-cell variation in the production process

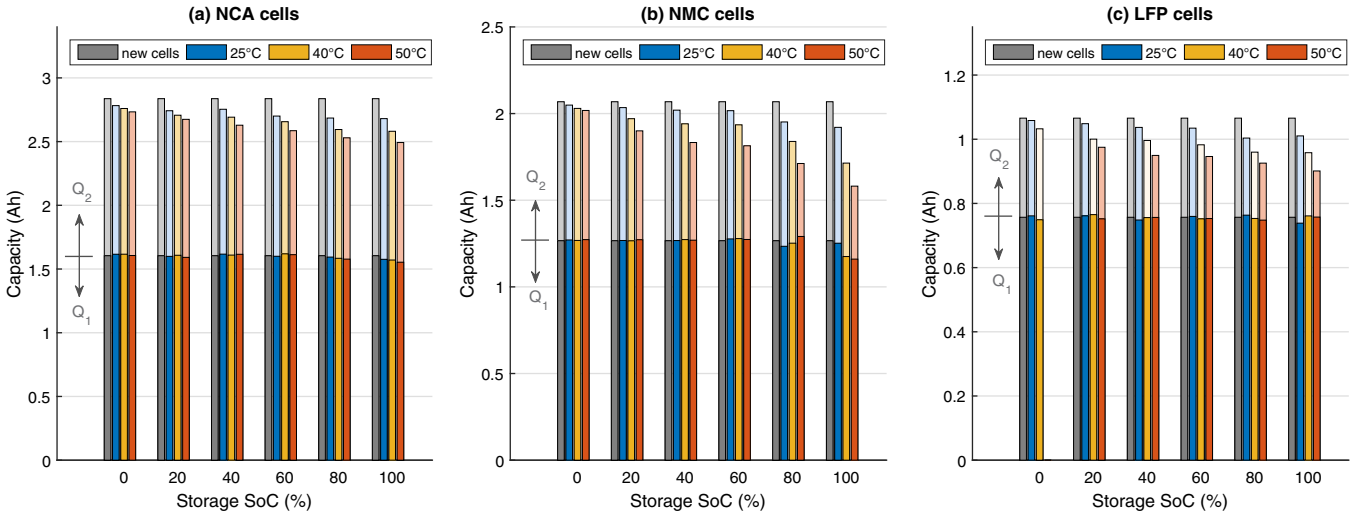

Figure 6. (a-c) Cell capacity after ca. 9–10 months of storage at different temperatures separated into characteristic capacities Q_1 and Q_2. The average value of all the new cells serves as the reference (gray bars).

for commercial 18650 lithium-ion cells. For the cells stored at 100% SoC, the differences in capacity fade should be minimal, as these cells had exactly the same test procedure. The remaining variations indicate that the effects of different charge-discharge history are less significant than those of the general cell-to-cell variation. Moreover, they are substantially smaller than the differences owing to the SoC. Thus, no different aging behavior is identified between the cells charged from 0% SoC to the storage SoC and the cells discharged from 100% SoC to the storage SoC. Thus, no effect due to the variations in lithium distribution or the open circuit voltage hysteresis resulting from different charge-discharge histories is detected.

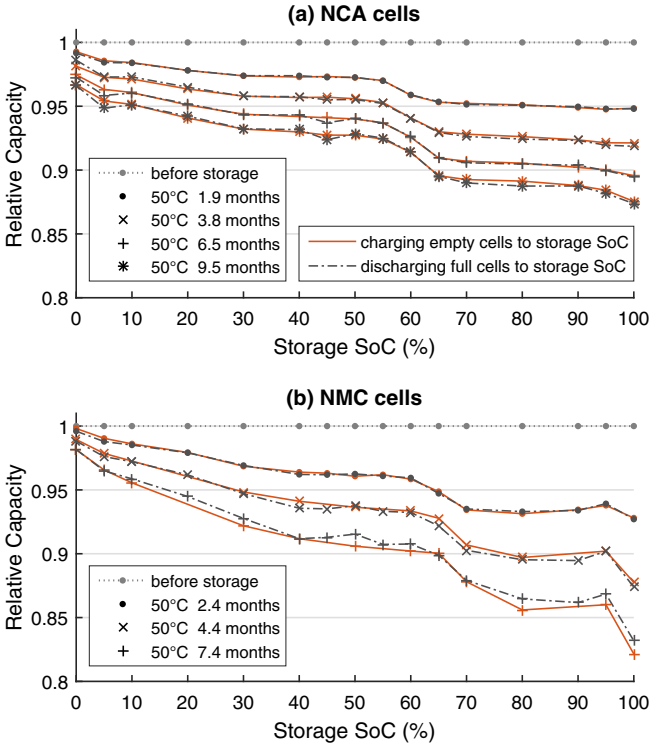

Figure 7. Comparison of capacity fade for the (a) NCA and (b) NMC cells stored at 50°C with different charge-discharge histories.

Impact of thickness changes.—Graphite anodes in lithium-ion batteries exhibit an expansion and contraction during lithiation and delithiation of 5%–10%.[51,52] Several researchers have suggested that SEI cracks and SEI reformation due to volume changes of the graphite anode during cycling operations are the major cause of lithium consumption.[28,53,54] Graphite anodes exhibit a largely linear expansion from 0% to 25% lithiation, only minor volume changes between 25% and 50% lithiation, and another linear expansion above 50% lithiation, where the LiC_6 phase formation begins.[52] Comparing this thickness behavior of lithiated graphite with the observed trends in capacity fade, an interdependency between graphite expansion and calendar aging can be disregarded: In the high SoC region above the central graphite peak, corresponding to a lithiation of the graphite anode greater than 50%, a constant capacity fade is observed. The thickness of the graphite anode, however, is continuously expanding above the central graphite peak. If the observed degradation was related to volume expansion, a continuously increasing degradation above the central graphite peak would be observed. Thus, it is not the expansion of the graphite causing the accelerated degradation at higher storage SoCs.

This confirms that the observed plateaus in capacity fade depend solely on the graphite potential and not on the thickness of the graphite electrode. Thus, the accelerated capacity fade above the central graphite peak is attributed to the lower anode potential, which aggravates electrolyte reduction and, thus, promotes SEI growth.

Transition zone at half-lithiated graphite anode.—In the capacity curves of Figures 2a–2c and Figures 5d–5f, a transition zone between moderate and high capacity fade has been observed around the central graphite peak. The high capacity fade occurs for storage SoCs above the peak location. These effects are now analyzed in more detail for the NCA cells. At 25°C, the transition zone remains unchanged for up to 9.5 months of storage. At 50°C, however, the transition zone widens.

Figure 8 demonstrates that this effect is a result of a change in electrode balancing, which shifts the SoC location of the central graphite peak toward higher SoCs. Figures 8a–8b confirm the capacity fade of the NCA cells stored at 25 and 50°C. The two cells stored at 60% SoC are highlighted. For these cells, Figures 8c–8d depict the corresponding differential voltage spectra for the different storage periods. The locations of the central graphite peak before the storage test and after about 9.5 months of storage are highlighted. The cells stored at 60% SoC were analyzed, since 60% SoC lies slightly above the location of the central graphite peak when the NCA cells are new. For storage at 25°C (Figure 8c), the location of the central graphite peak still remains

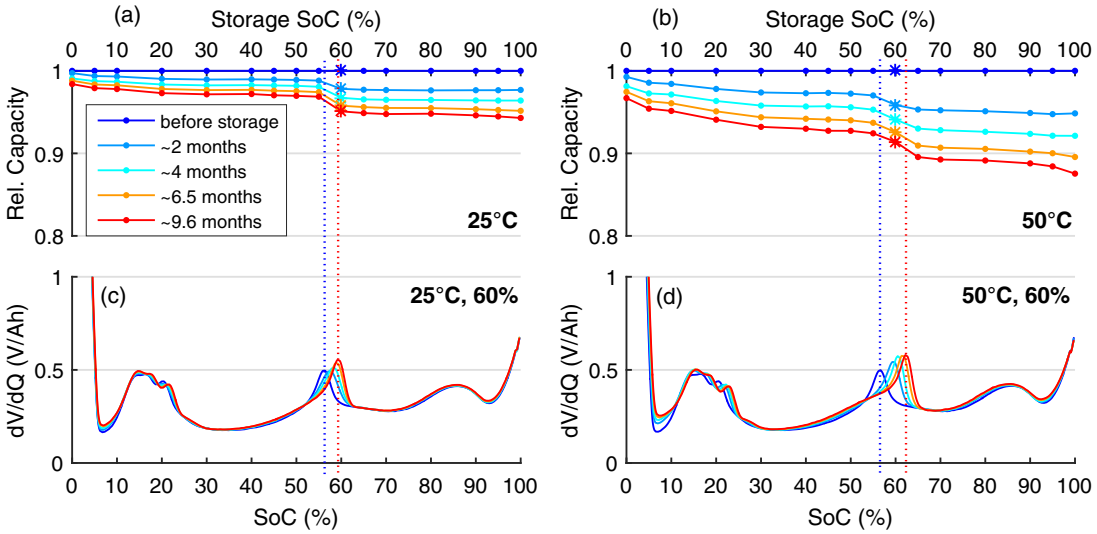

Figure 8. (a, b) Capacity fade over time for the NCA cells stored at 25 or 50°C. Cells stored at 60% are highlighted, for which (c, d) show the corresponding differential voltage spectra. The location of the central graphite peak is highlighted for the new state and that following ca. 9.5 months of storage.

below 60% SoC after 9.5 months of storage. Hence, the cell stored at 25°C and 60% SoC has always been in the plateau region of high capacity fade. Thus, the transition zone has remained between 55% and 60% SoC. For storage at 50°C (Figure 8d), a higher capacity fade occurs, which is caused by a greater loss of cyclable lithium. Due to the larger shift in the electrode balancing, the location of the central graphite peak lies above 60% SoC after only ca. 2 months of storage. Hence, the NCA cell stored at 50°C and 60% SoC exhibited high capacity fade only during the first weeks of storage and then slipped into the regime of medium capacity fade. Thus, only the cells stored at 65% SoC and above exhibit the fastest capacity fade. Consequently, the transition zone expands to 55%–65% SoC. This clear correlation between the balancing of the graphite anode and the capacity fade during storage periods confirms that the anode potential has been the major driving force of calendar aging in this study.

The identification and evaluation of a widening transition zone was only possible because storage SoCs related to the actual capacity were used instead of predefined voltage levels. They allowed the anode potential at the investigated storage SoCs to change with aging, which resulted in different aging rates over time for storage SoCs slightly above the initial SoC location of the central graphite peak.

Conclusions

Our experimental study of three different types of commercial lithium-ion cells has demonstrated that calendar aging does not increase steadily with the SoC. Instead, plateau regions, covering SoC intervals of more than 20%–30% of the cell capacity, have been observed in which the capacity fade is largely constant. In-depth analyses by DVA confirmed that the capacity fade is mainly caused by a shift in the electrode balancing and not by a degradation of the electrode materials.

Furthermore, our study revealed a strong dependency of calendar aging on the graphite electrode. Lower anode potentials were identified as the main driver of capacity fade during storage periods. In the high SoC regime where the graphite anode is lithiated more than 50%, the low anode potential accelerates the loss of cyclable lithium, causing the shift in the electrode balancing. The comparison of different types of lithium-ion cells demonstrated that the more the graphite anode is oversized, the higher the storage SoC can be without reaching the SoC regime of highest capacity fade.

The degradation due to the low anode potential can be attributed to electrolyte reduction and SEI growth. Signs of aging mechanisms induced by high cell voltage, such as electrolyte oxidation or transition-metal dissolution were observed only in few cases: A substantially accelerated capacity fade occurred for the NMC cells at 100% SoC. For the NCA cells, a storage SoC above 90% caused slightly increased battery aging. The aging behavior of the LFP cells correlates entirely with the anode potential. Moreover, no effects due to anode thickness or charge-discharge history on calendar aging were observed.

Overall, the effects from low graphite potential were predominant in our calendar aging study. To maximize battery life, lithium-ion cells should not be stored at high SoC corresponding to low anode potential. For long-term storage, the graphite anode should be lithiated less than 50%. To determine the respective SoC range of the full-cell, DVA provides the relevant characterization of the electrode balancing without opening the cells to insert a reference electrode or the need for post-mortem analyses.

References

1. A. J. Smith, H. M. Dahn, J. C. Burns, and J. R. Dahn, "Long-Term Low-Rate Cycling of $LiCoO_2$/Graphite Li-Ion Cells at 55°C," *J. Electrochem. Soc.*, **159**, A705 (2012).
2. T. Ohzuku, "Formation of Lithium-Graphite Intercalation Compounds in Nonaqueous Electrolytes and Their Application as a Negative Electrode for a Lithium Ion (Shuttlecock) Cell," *J. Electrochem. Soc.*, **140**, 2490 (1993).
3. W.-S. Yoon, K. Y. Chung, J. McBreen, and X.-Q. Yang, "A comparative study on structural changes of $LiCo_{1/3}Ni_{1/3}Mn_{1/3}O_2$ and $LiNi_{0.8}Co_{0.15}Al_{0.05}O_2$ during first charge using in situ XRD," *Electrochemistry Communications*, **8**, 1257 (2006).
4. W. H. Woodford, W. C. Carter, and Y.-M. Chiang, "Design criteria for electrochemical shock resistant battery electrodes," *Energy Environ. Sci.*, **5**, 8014 (2012).
5. B. Bitzer and A. Gruhle, "A new method for detecting lithium plating by measuring the cell thickness," *Journal of Power Sources*, **262**, 297 (2014).
6. C. Uhlmann, J. Illig, M. Ender, R. Schuster, and E. Ivers-Tiffée, "In situ detection of lithium metal plating on graphite in experimental cells," *Journal of Power Sources*, **279**, 428 (2015).
7. V. Zinth, C. von Lüders, M. Hofmann, J. Hattendorff, I. Buchberger, S. Erhard, J. Rebelo-Kornmeier, A. Jossen, and R. Gilles, "Lithium plating in lithium-ion batteries at sub-ambient temperatures investigated by in situ neutron diffraction," *Journal of Power Sources*, **271**, 152 (2014).
8. S. F. Schuster, T. Bach, E. Fleder, J. Müller, M. Brand, G. Sextl, and A. Jossen, "Nonlinear aging characteristics of lithium-ion cells under different operational conditions," *Journal of Energy Storage*, **1**, 44 (2015).
9. N. Legrand, B. Knosp, P. Desprez, F. Lapicque, and S. Raël, "Physical characterization of the charging process of a Li-ion battery and prediction of Li plating by electrochemical modelling," *Journal of Power Sources*, **245**, 208 (2014).
10. P. B. Balbuena and Y. Wang, *Lithium-ion batteries: Solid-electrolyte interphase*, Imperial College Press, London, 2004.
11. N. Dupré, J.-F. Martin, J. Oliveri, P. Soudan, A. Yamada, R. Kanno, and D. Guyomard, "Relationship between surface chemistry and electrochemical behavior of $LiNi_{1/2}Mn_{1/2}O_2$ positive electrode in a lithium-ion battery," *Journal of Power Sources*, **196**, 4791 (2011).

12. S.-P. Kim, A. C. van Duin, and V. B. Shenoy, "Effect of electrolytes on the structure and evolution of the solid electrolyte interphase (SEI) in Li-ion batteries: A molecular dynamics study," *Journal of Power Sources*, **196**, 8590 (2011).
13. M. Wohlfahrt-Mehrens, C. Vogler, and J. Garche, "Aging mechanisms of lithium cathode materials," *Journal of Power Sources*, **127**, 58 (2004).
14. J. Vetter, P. Novák, M. R. Wagner, C. Veit, K.-C. Möller, J. O. Besenhard, M. Winter, M. Wohlfahrt-Mehrens, C. Vogler, and A. Hammouche, "Ageing mechanisms in lithium-ion batteries," *Journal of Power Sources*, **147**, 269 (2005).
15. M. Broussely, P. Biensan, F. Bonhomme, P. Blanchard, S. Herreyre, K. Nechev, and R. J. Staniewicz, "Main aging mechanisms in Li ion batteries," *Journal of Power Sources*, **146**, 90 (2005).
16. I. Buchberger, S. Seidlmayer, A. Pokharel, M. Piana, J. Hattendorff, P. Kudejova, R. Gilles, and H. A. Gasteiger, "Aging Analysis of Graphite/$LiNi_{1/3}Mn_{1/3}Co_{1/3}O_2$ Cells Using XRD, PGAA, and AC Impedance," *J. Electrochem. Soc.*, **162**, A2737 (2015).
17. A. Funabiki, "Stage Transformation of Lithium-Graphite Intercalation Compounds Caused by Electrochemical Lithium Intercalation," *J. Electrochem. Soc.*, **146**, 2443 (1999).
18. I. Bloom, B. Cole, J. Sohn, S. Jones, E. Polzin, V. Battaglia, G. Henriksen, C. Motloch, R. Richardson, T. Unkelhaeuser, D. Ingersoll, and H. Case, "An accelerated calendar and cycle life study of Li-ion cells," *Journal of Power Sources*, **101**, 238 (2001).
19. J. Belt, V. Utgikar, and I. Bloom, "Calendar and PHEV cycle life aging of high-energy, lithium-ion cells containing blended spinel and layered-oxide cathodes," *Journal of Power Sources*, **196**, 10213 (2011).
20. S. Bourlot, P. Blanchard, and S. Robert, "Investigation of aging mechanisms of high power Li-ion cells used for hybrid electric vehicles," *Journal of Power Sources*, **196**, 6841 (2011).
21. S. Grolleau, A. Delaille, H. Gualous, P. Gyan, R. Revel, J. Bernard, E. Redondo-Iglesias, and J. Peter, "Calendar aging of commercial graphite/$LiFePO_4$ cell – Predicting capacity fade under time dependent storage conditions," *Journal of Power Sources*, **255**, 450 (2014).
22. M. Kassem, J. Bernard, R. Revel, S. Pélissier, F. Duclaud, and C. Delacourt, "Calendar aging of a graphite/$LiFePO_4$ cell," *Journal of Power Sources*, **208**, 296 (2012).
23. M. Kassem and C. Delacourt, "Postmortem analysis of calendar-aged graphite/$LiFePO_4$ cells," *Journal of Power Sources*, **235**, 159 (2013).
24. E. Sarasketa-Zabala, I. Gandiaga, L. M. Rodriguez-Martinez, and I. Villarreal, "Calendar ageing analysis of a $LiFePO_4$/graphite cell with dynamic model validations: Towards realistic lifetime predictions," *Journal of Power Sources*, **272**, 45 (2014).
25. B. Stiaszny, J. C. Ziegler, E. E. Krauß, M. Zhang, J. P. Schmidt, and E. Ivers-Tiffée, "Electrochemical characterization and post-mortem analysis of aged $LiMn_2O_4$–NMC/graphite lithium ion batteries part II: Calendar aging," *Journal of Power Sources*, **258**, 61 (2014).
26. M. Safari and C. Delacourt, "Aging of a Commercial Graphite/$LiFePO_4$ Cell," *J. Electrochem. Soc.*, **158**, A1123 (2011).
27. D. Li, D. L. Danilov, J. Xie, L. Raijmakers, L. Gao, Y. Yang, and P. H. Notten, "Degradation Mechanisms of C_6/$LiFePO_4$ Batteries: Experimental Analyses of Calendar Aging," *Electrochimica Acta*, **190**, 1124 (2016).
28. H. Zheng, L. Tan, L. Zhang, Q. Qu, Z. Wan, Y. Wang, M. Shen, and H. Zheng, "Correlation between lithium deposition on graphite electrode and the capacity loss for $LiFePO_4$/graphite cells," *Electrochimica Acta*, **173**, 323 (2015).
29. S. Käbitz, J. B. Gerschler, M. Ecker, Y. Yurdagel, B. Emmermacher, D. André, T. Mitsch, and D. U. Sauer, "Cycle and calendar life study of a graphite|$LiNi_{1/3}Mn_{1/3}Co_{1/3}O_2$ Li-ion high energy system. Part A: Full cell characterization," *Journal of Power Sources*, **239**, 572 (2013).
30. M. Ecker, N. Nieto, S. Käbitz, J. Schmalstieg, H. Blanke, A. Warnecke, and D. U. Sauer, "Calendar and cycle life study of Li(NiMnCo)O_2-based 18650 lithium-ion batteries," *Journal of Power Sources*, **248**, 839 (2014).
31. V. Pop, H. J. Bergveld, P. P. L. Regtien, Op het Veld, J. H. G. , D. Danilov, and P. H. L. Notten, "Battery Aging and Its Influence on the Electromotive Force," *J. Electrochem. Soc.*, **154**, A744 (2007).
32. M. M. Doeff and Battery Cathodes, in: R. J. Brodd (Ed.), *Batteries for Sustainability*, Springer, New York, NY, 2013, pp. 5.
33. P. Keil and A. Jossen, "Charging Protocols for Lithium-Ion Batteries and their Impact on Cycle Life - An Experimental Study with Different 18650 High-Power Cells," *Journal of Energy Storage* in press.
34. P. Keil and A. Jossen, *Aging of Lithium-Ion Batteries in Electric Vehicles: Impact of Regenerative Braking, Electric Vehicle Symposium (EVS28)*, Goyang, Korea, 2015.
35. I. Bloom, A. N. Jansen, D. P. Abraham, J. Knuth, S. A. Jones, V. S. Battaglia, and G. L. Henriksen, "Differential voltage analyses of high-power, lithium-ion cells," *Journal of Power Sources*, **139**, 295 (2005).
36. H. M. Dahn, A. J. Smith, J. C. Burns, D. A. Stevens, and J. R. Dahn, "User-Friendly Differential Voltage Analysis Freeware for the Analysis of Degradation Mechanisms in Li-Ion Batteries," *Journal of the Electrochemical Society*, **159**, A1405 (2012).
37. M. Dubarry, C. Truchot, and B. Y. Liaw, "Synthesize battery degradation modes via a diagnostic and prognostic model," *Journal of Power Sources*, **219**, 204 (2012).
38. K. Honkura and T. Horiba, "Study of the deterioration mechanism of LiCoO2/graphite cells in charge/discharge cycles using the discharge curve analysis," *Journal of Power Sources*, **264**, 140 (2014).
39. A. K. Sleigh, J. J. Murray, and W. R. McKinnon, "Memory effects due to phase conversion and hysteresis in Li/$LixMnO_2$ cells," *Electrochimica Acta*, **36**, 1469 (1991).
40. W. Dreyer, C. Guhlke, and R. Huth, "The behavior of a many-particle electrode in a lithium-ion battery," *Physica D: Nonlinear Phenomena*, **240**, 1008 (2011).
41. M. Hess, *Kinetics and stage transitions of graphite for lithium-ion batteries*, Zürich, ETH / PSI, 2013.
42. A. Barai, W. D. Widanage, J. Marco, A. McGordon, and P. Jennings, "A study of the open circuit voltage characterization technique and hysteresis assessment of lithium-ion cells," *Journal of Power Sources*, **295**, 99 (2015).
43. D. Manka and E. Ivers-Tiffée, "Electro-optical measurements of lithium intercalation/de-intercalation at graphite anode surfaces," *Electrochimica Acta*, **186**, 642 (2015).
44. Y. Lee, B. Son, J. Choi, J. H. Kim, M.-H. Ryou, and Y. M. Lee, "Effect of back-side-coated electrodes on electrochemical performances of lithium-ion batteries," *Journal of Power Sources*, **275**, 712 (2015).
45. H. He, C. Huang, C.-W. Luo, J.-J. Liu, and Z.-S. Chao, "Dynamic study of Li intercalation into graphite by in situ high energy synchrotron XRD," *Electrochimica Acta*, **92**, 148 (2013).
46. Y. Itou and Y. Ukyo, "Performance of $LiNiCoO_2$ materials for advanced lithium-ion batteries," *Journal of Power Sources*, **146**, 39 (2005).
47. W.-J. Zhang, "Structure and performance of LiFePO4 cathode materials: A review," *Journal of Power Sources*, **196**, 2962 (2011).
48. C. Masquelier, S. Patoux, C. Wurm, and M. Morcrette, *Polyanion-Based Positive Electrode Materials*, in: G.-A. Nazri and G. Pistoia (Eds.), Lithium Batteries, Springer US, Boston, MA, 2003, pp. 445.
49. M. Broussely, S. Herreyre, P. Biensan, P. Kasztejna, K. Nechev, and R. Staniewicz, "Aging mechanism in Li ion cells and calendar life predictions," *Journal of Power Sources*, **97–98**, 13 (2001).
50. H. J. Ploehn, P. Ramadass, and R. E. White, "Solvent Diffusion Model for Aging of Lithium-Ion Battery Cells," *J. Electrochem. Soc.*, **151**, A456 (2004).
51. M. Winter, G. H. Wrodnigg, J. O. Besenhard, W. Biberacher, and P. Novák, "Dilatometric Investigations of Graphite Electrodes in Nonaqueous Lithium Battery Electrolytes," *J. Electrochem. Soc.*, **147**, 2427 (2000).
52. B. Rieger, S. Schlueter, S. V. Erhard, J. Schmalz, G. Reinhart, and A. Jossen, "Multi-scale investigation of thickness changes in a commercial pouch type lithium-ion battery," *Journal of Energy Storage*, **6**, 213 (2016).
53. I. Laresgoiti, S. Käbitz, M. Ecker, and D. U. Sauer, "Modeling mechanical degradation in lithium ion batteries during cycling: Solid electrolyte interphase fracture," *Journal of Power Sources*, **300**, 112 (2015).
54. R. Deshpande, M. Verbrugge, Y.-T. Cheng, J. Wang, and P. Liu, "Battery Cycle Life Prediction with Coupled Chemical Degradation and Fatigue Mechanics," *Journal of the Electrochemical Society*, **159**, A1730 (2012).